



Superior photoelectrocatalytic performance of Mo-doped γ -Fe₂O₃ catalyst for degrading tetracycline

Xinyu Xia¹, Zihan Zhang¹, Peng Jia¹, Huili Wang¹, Wenxia Liu¹, Xiaona Liu^{1,*}, Zhendong Liu^{2,*}

Keywords:

Photoelectrocatalytic, Mo-Fe₂O₃, doped catalyst, tetracycline, electronic interactions

Citation:

Xia, X.; Zhang, Z.; Jia, P.; Wang, H.; Liu, W.; Liu, X.; Liu, Z. Superior photoelectrocatalytic performance of Mo-doped γ -Fe₂O₃ catalyst for degrading tetracycline. *Energy Mater.* 2026, 6, 600052. <https://dx.doi.org/10.20517/energymater.2026.17>

Received: 2 Feb 2026

First Decision: 24 Mar 2026

Revised: 6 May 2026

Accepted: 13 May 2026

Published: 21 May 2026

Academic Editor:

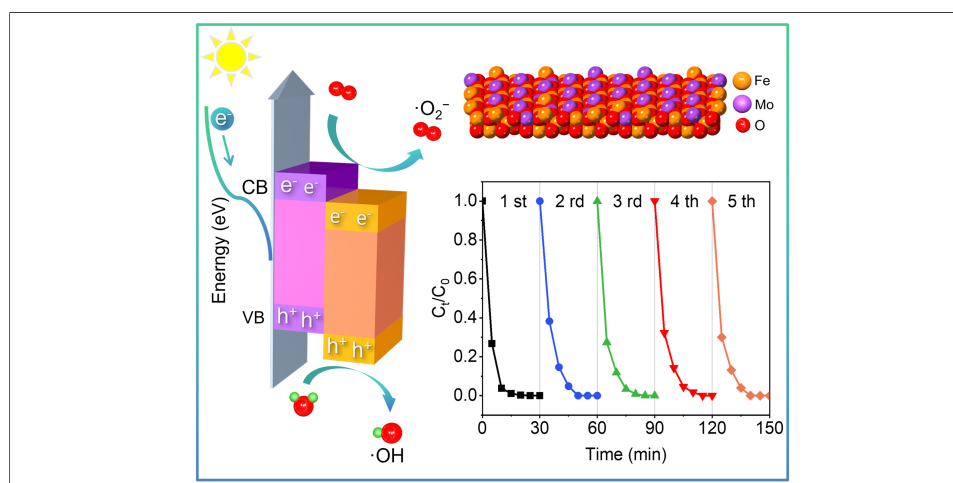
Ho Won Jang

Copy Editor:

Ping Zhang

Production Editor:

Ping Zhang



Abstract

Photoelectrocatalytic (PEC) technology is one of the effective methods for degrading tetracycline (TC) in wastewater. In this work, we designed a doping system by incorporating Mo atoms into the lattice of γ -Fe₂O₃ and achieved a generic characteristic of superior PEC activity. Mo atoms are proven to be doped into the lattice of γ -Fe₂O₃ through the analysis of X-ray diffraction (XRD), X-ray photoelectron spectra (XPS), transmission electron microscope energy dispersive X-ray spectroscopy (TEM-EDS) mapping and high-angle annular dark-field scanning transmission electron microscopy (HAADF-STEM). Valence band XPS and ultraviolet photoelectron spectroscopy (UPS) measurements reveal that the Mo doping can affect the electronic structure of γ -Fe₂O₃, enhancing the electronic interactions, facilitating the separation and transformation of photogenerated charges, and resulting in the superior PEC activity. 27% Mo-Fe₂O₃ exhibits excellent photoelectrochemical properties and reaches the removal efficiency of 100% in 25 min for degrading TC. Thus, this work provides a feasible strategy for developing doped catalysts with superior PEC performance by enhancing the electronic interactions.



¹State Key Laboratory of Green Papermaking and Resource Recycling, Faculty of Light Industry, Qilu University of Technology, Shandong Academy of Sciences, Jinan 250353, Shandong, China.

²Shandong Environmental Protection Development Group Co., Ltd., Jinan 250101, Shandong, China.

*Correspondence to: Dr. Xiaona Liu, State Key Laboratory of Green Papermaking and Resource Recycling, Faculty of Light Industry, Qilu University of Technology, Shandong Academy of Sciences, Jinan 250353, Shandong, China. E-mail: liuxn0107@126.com; Dr. Zhendong Liu, Shandong Environmental Protection Development Group Co., Ltd., Jinan 250101, Shandong, China. E-mail: lzd100820@163.com

INTRODUCTION

Along with the rapid development of the global social economy in recent decades, the consumption of antibiotics has been continuously increasing^[1]. Tetracycline (TC) is a typical broad-spectrum antibiotic that has been widely and increasingly used in human medicine, livestock farming, and aquaculture^[2–4]. Generally speaking, only less than 30% of the administered antibiotic dosage can be absorbed and metabolized by humans and animals^[5], while the rest are excreted into the environment where they persist and spread, posing a potential threat to the ecosystem and human health. Owing to its high chemical stability, TC exhibits a prolonged half-life and is difficult to be naturally decomposed in the environment^[6]. Conventional treatment methods are limited by their inherent limitations. For example, physical adsorption and activated sludge technology primarily rely on adsorption mechanisms and cannot completely remove TC^[7,8]. Biodegradation technology is an eco-friendly treatment approach, while can not rapidly eliminate TC due to its slow degradation kinetics^[9]. Therefore, it is urgent to develop a rapid and thorough technology for removing TC. Photocatalysis, driven by solar energy, is regarded as a promising technology for degrading TC effectively in wastewater owing to its advantages such as low energy consumption and high efficiency^[10–12]. However, the photocatalytic technology is constrained by the low utilization rate of solar energy and the rapid recombination of photogenerated charges^[13–15]. Photoelectrocatalytic (PEC), combining photochemical and electrochemical oxidation by applying an external bias, is an effective method that promotes the separation and transfer of photogenerated charges, reducing recombination losses, and enhancing the generation of reactive species^[16]. Some transition-metal oxides such as TiO_2 , WO_3 , and ZnO have been widely researched as photocatalysts, while their large band gap and rapid recombination of photogenerated carriers lead to low PEC efficiency^[17–19]. To overcome these limitations, strategies such as heterojunction construction^[20], defect engineering^[21], and nanostructure regulation^[22] have been employed to enhance their PEC performance. Yu *et al.* synthesized an S-scheme $2\text{H-MoSe}_2/\text{NiFe-LDH}$ heterojunction photoanode showing excellent TC degradation performance, retained over 95% efficiency across 10 cycles, attributed to the efficient separation and utilization of photogenerated electrons and holes^[23]. Liu *et al.* constructed a novel photoelectrocatalysis/photoelectro-Fenton system by coupling a cone-like TiO_2 photoanode grown on nickel foam with a natural air-diffusion electrode, achieved complete removal of carbamazepine in 30 min, and revealed the synergistic mechanism of enhanced H_2O_2 production and direct hole oxidation^[24]. Li *et al.* observed the efficient spatial separation and transfer of photoinduced charges in a ferroelectric-polarized $\text{TiO}_2/\text{BaTiO}_3$ heterostructure using single-particle imaging technology directly, revealing the critical role of the polarization orientation in enhancing the piezoelectric-photocatalytic performance^[25]. Vaghasiya *et al.* developed a $\text{g-C}_3\text{N}_4$ -based magnetic soft centirobot that generates reactive oxygen species under black light illumination to efficiently kill bacteria in water, demonstrating the potential of photoactive materials for mitigating biological threats^[26]. Hu *et al.* developed a chlorine-doped pentagonal defect-rich nanocarbon catalyst that enables efficient H_2O_2 electrosynthesis in seawater and achieves rapid degradation of tetracycline, further demonstrating the potential of electrocatalytic reactive oxygen species generation for antibiotic removal^[27].

Maghemite ($\gamma\text{-Fe}_2\text{O}_3$), an eco-friendly semiconductor material, has been applied extensively in the catalytic field because of its appropriate band gap characteristics, high chemical stability, and excellent magnetic properties. While due to the fast recombination of photogenerated charges, $\gamma\text{-Fe}_2\text{O}_3$ has relatively poor photocatalytic efficiency. To address this issue, the doping strategy provides a novel approach for optimizing catalyst performance. Compared with cocatalyst loading or heterojunction construction using metal carbides^[28], doping offers unique advantages in modulating electronic band structures and introducing stable active sites within the lattice. Kahng and Kim have reported a $\text{SnO}_2/\text{Mo-doped BiVO}_4$ heterojunction photoanode, in which Mo doping enhances n-type conductivity and the SnO_2 layer blocks hole recombination, thereby achieving efficient photoelectrochemical degradation of tetracycline hydrochloride^[29]. Zhang *et al.* have reported a $\text{MoO}_3/\text{Mo-doped BiOCl}$ Ohmic junction with abundant

oxygen vacancies, in which the Mo doping induces oxygen vacancies and the MoO₂ cocatalyst promotes charge carrier separation, thereby achieving efficient photocatalytic degradation of tetracycline hydrochloride^[30].

In this work, we designed a doping system by incorporating Mo atoms into the lattice of γ -Fe₂O₃ and achieved a generic characteristic of superior PEC activity. Mo atoms are proved to be incorporated into the lattice of γ -Fe₂O₃ in the form of doping through the analysis of X-ray diffraction (XRD), X-ray photoelectron spectra (XPS) and high-angle annular dark-field scanning transmission electron microscopy (HAADF-STEM). The modification of Mo doping can affect the electron cloud structure of γ -Fe₂O₃, enhancing the electronic interactions, facilitating the separation and transformation of photogenerated charges, and resulting in the superior PEC activity. The 27% Mo-doped γ -Fe₂O₃ exhibits excellent photoelectrochemical properties, such as the lowest onset potential of -0.7 V, an enhanced photocurrent density as high as -184 mA·cm⁻² at the potential of -1.5 V versus reversible hydrogen electrode (vs. RHE), and reaches the removal efficiency of 100% in 25 min for degrading TC. Thus, this work provides a feasible strategy for developing doped catalysts with superior PEC performance by enhancing the electronic interactions.

EXPERIMENTAL

Materials

All chemicals were purchased in analytical grade and used without any further treatment. (NH₄)₆Mo₇O₂₄·4H₂O, C₂H₂O₄·2H₂O, NaOH, Na₂SO₄, FeSO₄·7H₂O, and CH₃OH were purchased from Sinopharm Chemical Reagent Co., Ltd. (Shanghai, China). p-Benzoquinone (PBQ, 99%), KBrO₃, ethylenediaminetetraacetic acid disodium salt dihydrate (EDTA-2Na), FeCl₃·6H₂O, isopropanol (IPA, 99.5%), and tetracycline (TC, CAS: 60-54-8) were purchased from Macklin Biochemical Technology Co., Ltd. (Shanghai, China). Nafion solution (5 wt%) and hydrophilic carbon cloth were purchased from Suzhou Sunernuo Technology Co., Ltd. (Suzhou, China).

Syntheses of γ -Fe₂O₃ and α -MoO₃

The synthesis of γ -Fe₂O₃ was carried out using a modified version of a literature method^[31]. The specific procedures were as follows: 2.70 g of FeCl₃·6H₂O and 5.56 g of FeSO₄·7H₂O were dissolved together in 100 mL of deionized water under vigorous magnetic stirring until completely dissolved, to which 1 mol·L⁻¹ NaOH was added under stirring until the pH reached 9 and kept stirring for 2 h. The precipitate was washed with deionized water three times, separated and collected by centrifugation, and dried at 80 °C for 12 h. Finally, γ -Fe₂O₃ was obtained after being calcined at 300 °C for 3 h in air and 500 °C for 3 h in Ar. α -MoO₃ was synthesized by calcining (NH₄)₆Mo₇O₂₄·4H₂O in air at 500 °C for 3 h.

Syntheses of Mo-Fe₂O₃

The Mo-Fe₂O₃ were prepared via an impregnation method. Firstly, a certain amount (0.1, 0.2, 0.3, 0.4 and 0.5 g) of (NH₄)₆Mo₇O₂₄·4H₂O was dissolved in deionized water, and then γ -Fe₂O₃ powder (1.00 g) was added under vigorous magnetic stirring at 80 °C until the water was fully evaporated. Then, the mixture was dried and calcined according to the synthesis of γ -Fe₂O₃. Finally, the obtained samples were recorded as x% Mo-Fe₂O₃. Herein, x% stands for the molar ratios of Mo to γ -Fe₂O₃ (x = 9, 18, 27, 36, and 45).

Fabrication of photocathodes

The fabrication method of one photocathode was improved according to the report^[32]. Specifically, 2.0 mg of sample, 350 μ L of ethanol, and 50 μ L of Nafion solution (5 wt%) were added to 600 μ L of deionized water and ultrasonicated for 0.5 h to form a homogeneous ink with a mass concentration of 2.0 mg·mL⁻¹. Then, 250 μ L of the as-prepared ink was coated onto a 1.0 cm × 1.4 cm hydrophilic carbon cloth (the actual exposed area

mounted on the electrode clamp was exactly $1.0\text{ cm} \times 1.0\text{ cm}$). Finally, the fabricated photoelectrode with a loading amount of $0.357\text{ mg}\cdot\text{cm}^{-2}$ was dried at $60\text{ }^{\circ}\text{C}$ for 3 h. For the convenience of description, the fabricated electrodes with $\gamma\text{-Fe}_2\text{O}_3$ and $x\%$ Mo- Fe_2O_3 ($x = 9, 18, 27, 36$, and 45) were marked as S_0, S_1, S_2, S_3, S_4 and S_5 , respectively.

Structural characterization

XRD data was collected from 20° to 80° at a scan rate of $20^{\circ}\cdot\text{min}^{-1}$ on a X-ray diffractometer (Rigaku SmartLab SE, Japan) under a $\text{Cu K}\alpha$ radiation power of $50\text{ kV} \times 44\text{ mA}$ to identify the crystal structure of each photoelectrocatalyst. Aberration-corrected high-angle annular dark-field scanning transmission electron microscopy (AC-HAADF-STEM) was observed by Thermo Scientific Themis Z transmission electron microscope equipped with dual spherical aberration correctors. Transmission electron microscope energy dispersive X-ray spectroscopy (TEM-EDS) elemental mapping was performed on a Thermo Scientific Talos F200S transmission electron microscope. XPS were recorded on a Thermo Scientific ESCALAB Xi+ spectrometer with a monochromatic $\text{Al K}\alpha$ source to determine the surface chemical composition. The high-resolution XPS spectra were acquired at a pass energy of 150.0 eV and a step size of 1.0 eV to analyze the chemical states of surface elements. All binding energies were calibrated with the adventitious carbon C 1s peak at 284.8 eV . Valence band XPS spectra were also collected on a Thermo Scientific K-Alpha spectrometer under the same experimental conditions. The valence band maximum (VBM) was determined by linear extrapolation of the leading edge of the valence band spectrum to the baseline. Ultraviolet photoelectron spectroscopy (UPS) measurements were performed on a Thermo Fisher Scientific ESCALAB Xi using a He I ($h\nu = 21.22\text{ eV}$) source. A silver reference sample was used to calibrate the binding energy scale ($E_{\text{Fermi}} = 0\text{ eV}$). UPS spectra were collected under a bias of -5 V for the secondary electron cutoff region. The work function (Φ) was calculated using the formula $\Phi = h\nu - (E_{\text{cutoff}} - E_{\text{Fermi}})$, where E_{cutoff} was determined by linear extrapolation of the secondary electron cutoff edge^[33]. The ultraviolet-visible (UV-Vis) diffuse reflectance spectra (UV-Vis DRS) were collected from 300 nm to 800 nm on a Shimadzu UV-2600 spectrophotometer equipped with an integrating sphere, in which BaSO_4 acts as a reference of 100% reflectance to analyze the light absorption properties of photoelectrocatalysts. Inductively coupled plasma optical emission spectrometry (ICP-OES) analysis was carried out on an Agilent 5110 inductively coupled plasma optical emission spectrometer (Agilent Technologies, USA). The radio frequency power was set to $1,300\text{ W}$, the nebulizer gas flow rate was $0.6\text{ L}\cdot\text{min}^{-1}$, the sample uptake delay was 9 s , the instrument stabilization delay was 7 s , and the replicate read time was 8 s .

Electrochemical characterization

All the electrochemical properties were evaluated in $0.25\text{ M Na}_2\text{SO}_4$ solution on a CHI 660E electrochemical workstation (Chenhua, Shanghai, China). The three-electrode system was assembled with one photocathode as working electrode, a Pt plate as counter electrode, and a saturated calomel electrode (SCE) as a reference electrode. The linear sweep voltammogram (LSV) curves at the scan rate of $10\text{ mV}\cdot\text{s}^{-1}$ and I-t curves under chopped light were obtained under AM 1.5 G illumination ($100\text{ mW}\cdot\text{cm}^{-2}$). The transient photocurrent responses (I-t curves) were recorded at a constant applied potential of -0.1 V vs. SCE under chopped light illumination (light/dark cycles) with the same light source. The electrochemical impedance spectroscopy (EIS) data was collected at a central potential of 0 V vs. RHE with an AC amplitude of 5 mV in the frequency range from 100 kHz to 0.1 Hz . The Mott-Schottky analysis was carried out in a potential range from -1.0 V to 0.5 V vs. RHE under a frequency of 1 kHz in dark. The cyclic voltammetry (CV) curves for double-layer capacitance (C_{dl}) were recorded at the scan rates ranging from $10\text{ mV}\cdot\text{s}^{-1}$ to $100\text{ mV}\cdot\text{s}^{-1}$ within a non-Faradaic potential window of $0.665\text{--}0.765\text{ V vs. RHE}$. All measured potentials were converted to the reversible hydrogen electrode potential (V vs. RHE) according to $E_{\text{RHE}} = E_{\text{SCE}} + 0.241 + 0.059 \times \text{pH}$ ^[34]. In this work, the electrolyte was air-saturated without additional O_2 bubbling, and its pH was equal to 6.8.

PEC of TC

The TC degradation performance of each photocathode was evaluated at a potential of -1.5 V (vs. RHE) in a single-compartment three-electrode quartz electrolytic cell, which was under the magnetic stirring and exposed to a 300 W Xe lamp with an optical filter ($\lambda > 420$ nm). The reaction solutions composed of TC (an initial concentration of 10, 50 or 100 mg·L⁻¹, namely ppm; an initial volume of 40 mL) and 0.25 M Na₂SO₄ were taken 1.5 mL every 5 min over the 30 min reaction period. All degradation experiments were performed in three times under identical conditions. The data are presented as mean \pm standard deviation (SD), and the error bars in the corresponding figures represent the SD of three independent measurements. The analysis method for TC was modified based on the previous report^[35]. The TC concentration was determined at a detection wavelength of 365 nm by an UltiMate 3000 high-performance liquid chromatography (HPLC) system equipped with a C18 column, in which the mobile phase (25 wt% methanol and 75 wt% 0.01 M oxalic acid aqueous solution) flowed at a rate of 0.8 mL·min⁻¹ at 35 °C, and the injection volume of taken reaction solution was 25 μ L. The intermediate products during TC degradation were detected and identified by a liquid chromatography-mass spectrometry (LC-MS, Agilent 1290 UPLC and Agilent 6550 Q-TOF) under the the electrospray ionization in positive ion mode (ESI⁺), equipped with a C18 column (100 mm \times 2.1 mm, 1.7 μ m). This work used a gradient elution program, in which the mobile phase consisted of 0.1 wt% formic acid in a mixture of 90 mL water and 10 mL acetonitrile and flowed at a rate of 0.3 mL·min⁻¹ at 35 °C, and the injection volume was 3 μ L.

RESULTS AND DISCUSSION

The XRD patterns of γ -Fe₂O₃ and $x\%$ Mo-Fe₂O₃ are shown in Figure 1. All diffraction peaks of γ -Fe₂O₃ match well with the standard data of the cubic spinel structure (JCPDS No. 39-1346)^[36], without any impurity peaks. As the doping amount of Mo increases to 27%, the crystal structure of $x\%$ Mo-Fe₂O₃ remains the cubic spinel structure. Notably, in the magnified patterns of the (311) peak of the γ -Fe₂O₃ phase, the diffraction peak shifts from 35.63° to 35.75°, illustrating that Mo ions successfully insert into the lattice of the γ -Fe₂O₃ crystal structure^[37]. When the doping amount of Mo exceeds 27%, the orthorhombic α -MoO₃ phase (JCPDS No. 73-6497, shown in Supplementary Figure 1) forms, demonstrating that the maximum doping amount of Mo should not exceed 27% to ensure the existence of Mo as the dopant incorporated into the γ -Fe₂O₃ lattice. To provide the actual Mo doping content, ICP-OES analysis was performed on the 27% sample. As listed in Supplementary Table 1, the actual molar ratio of Mo to γ -Fe₂O₃ is 33.32%, which is slightly higher than the nominal theoretical ratio of 27%, and this small deviation is attributed to the methodological error of the ICP-OES analysis.

AC-HAADF-STEM was used to directly observe the surface Mo species in the 27% Mo-Fe₂O₃. As shown in Figure 2A, the measured interplanar spacing of 2.5 Å was assigned to the (311) lattice plane of γ -Fe₂O₃^[38], consistent with XRD spectra. In AC-HAADF-STEM imaging mode, the image intensity is approximately proportional to the square of the atomic number (Z^2). There are some bright flecks detected in the uniform arrangement of the γ -Fe₂O₃ crystallites, attributed to isolated Mo atoms highlighted by red dashed circles. Therefore, Mo atoms coordinated with O are doped into the lattice of γ -Fe₂O₃ successfully. As further analyzed by the selected-area intensity surface plot and the corresponding structural model in Figure 2B and C, there are image intensity variations existed in the γ -Fe₂O₃ lattice and all the Mo atoms with high contrast are located in the lattice sites, confirming the Mo atoms are anchored on the Fe hollow sites in the γ -Fe₂O₃ lattice structure. Moreover, no Mo nanoclusters or nanoparticles are observed in multiple regions of the 27% Mo-Fe₂O₃, and the corresponding Mo elemental maps exhibit a uniform distribution [Supplementary Figure 2]. Combined with the AC-HAADF-STEM image in Figure 2, these results indicate that the Mo species are incorporated into the γ -Fe₂O₃ lattice as dopants.

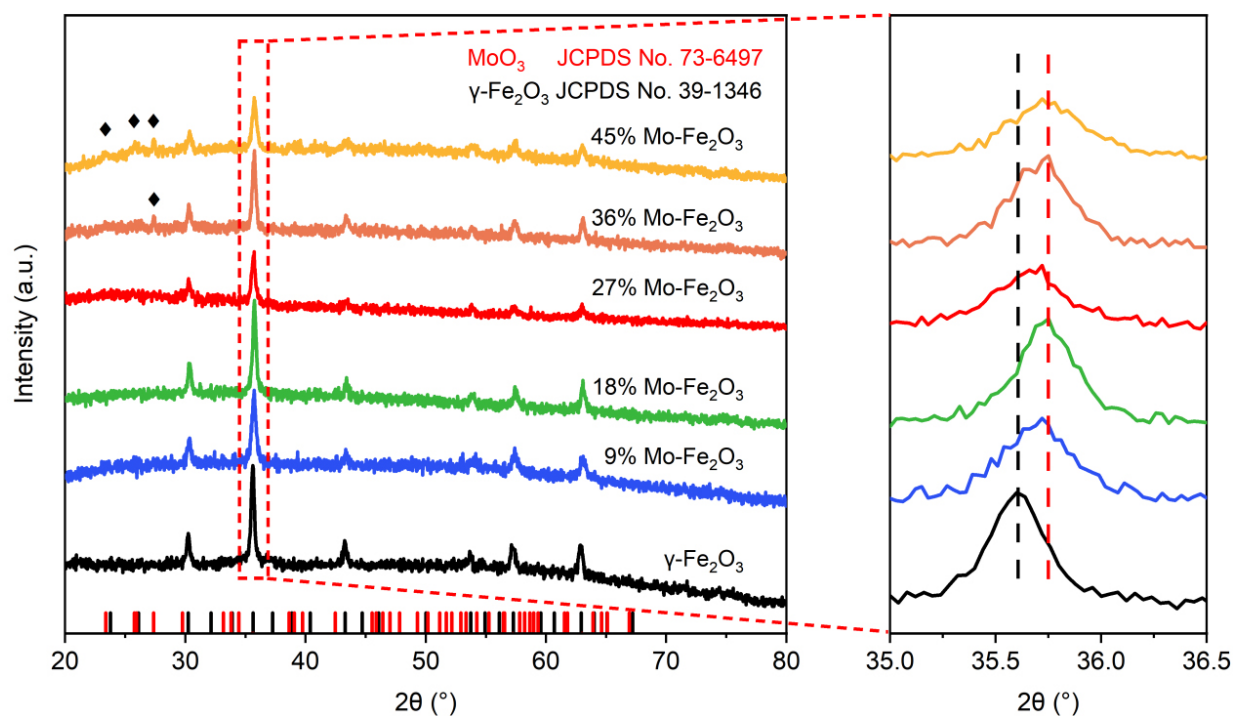


Figure 1. XRD patterns of γ - Fe_2O_3 , 9% $\text{Mo-Fe}_2\text{O}_3$, 18% $\text{Mo-Fe}_2\text{O}_3$, 27% $\text{Mo-Fe}_2\text{O}_3$, 36% $\text{Mo-Fe}_2\text{O}_3$, and 45% $\text{Mo-Fe}_2\text{O}_3$, respectively. In the panel, the diffraction peaks (\blacklozenge) are assigned to the α - MoO_3 phase, and the short vertical lines below the XRD patterns mark all Bragg positions of γ - Fe_2O_3 (black) and MoO_3 (red). XRD patterns on the right are the magnified of the (311) peak of the γ - Fe_2O_3 phase in the dashed box. XRD: X-ray diffraction.

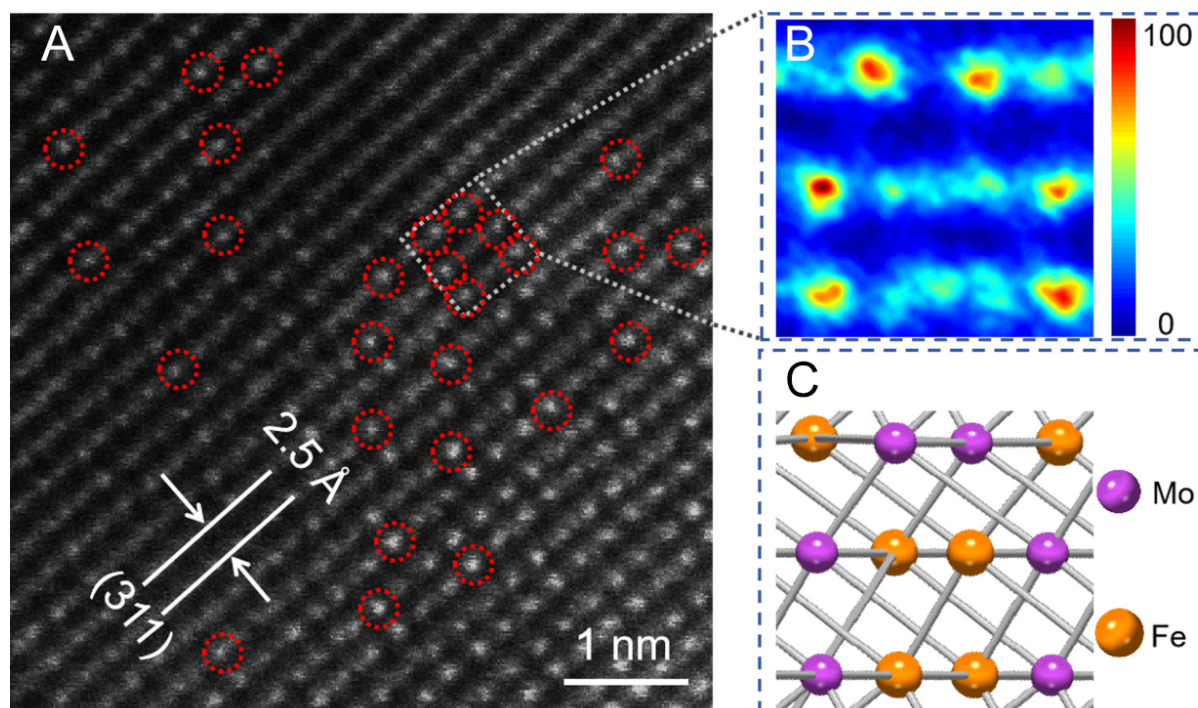


Figure 2. (A) AC-HAADF-STEM image of 27% $\text{Mo-Fe}_2\text{O}_3$; (B) Surface intensity profile and (C) the corresponding structural model of the selected area (blue dashed square area in A). Insets in (C): The purple and orange balls represent Mo and Fe atoms, respectively. AC-HAADF-STEM: Aberration-corrected high-angle annular dark-field scanning transmission electron microscopy.

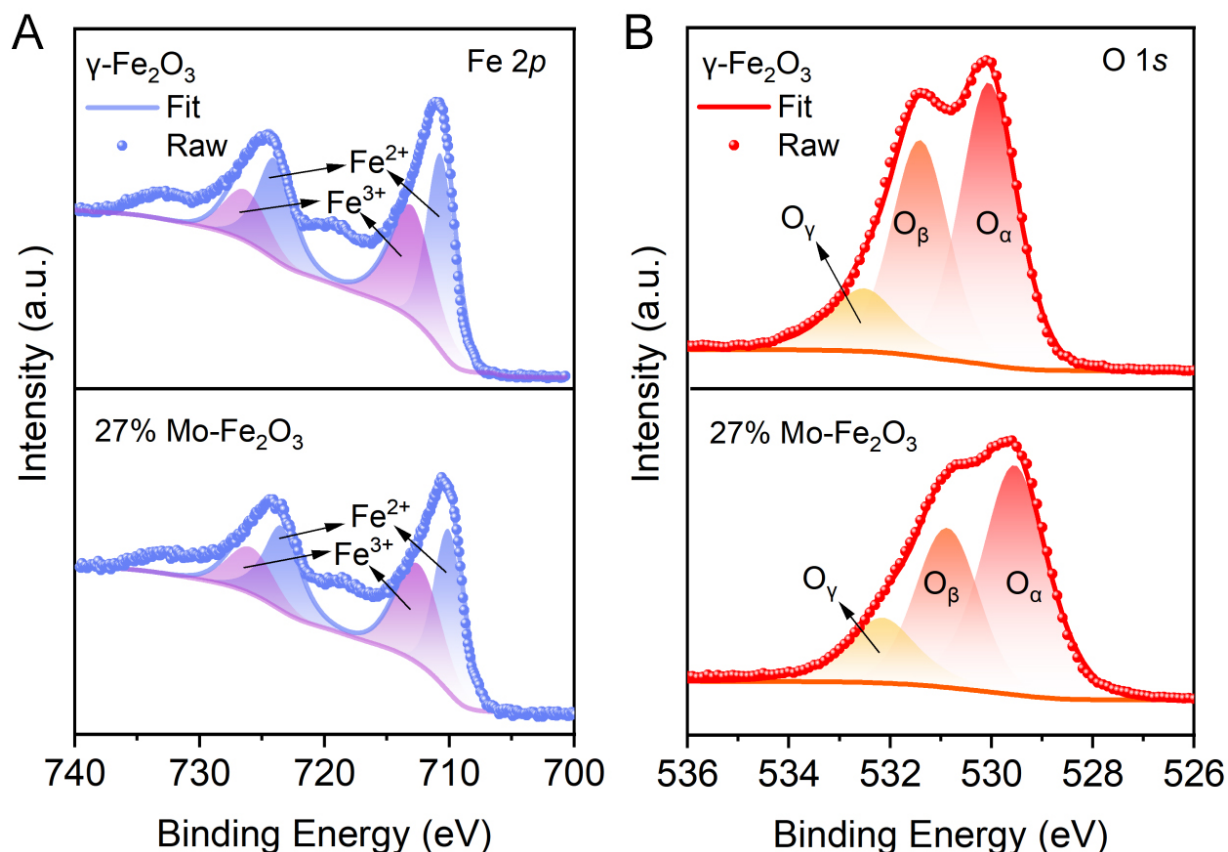


Figure 3. High-resolution (A) Fe 2p and (B) O 1s XPS spectra of $\gamma\text{-Fe}_2\text{O}_3$ and 27% Mo- Fe_2O_3 . XPS: X-ray photoelectron spectra.

We investigate the surface chemical states of $\gamma\text{-Fe}_2\text{O}_3$ and 27% Mo- Fe_2O_3 by XPS [Figure 3 and Supplementary Table 2]. Figure 3A shows the high-resolution Fe 2p XPS spectra with two spin-splitting bands of Fe $2p_{3/2}$ and $2p_{1/2}$, both of which are fitted into two peaks: 710.7 ($\text{Fe}^{2+} 2p_{3/2}$), 713.0 ($\text{Fe}^{3+} 2p_{3/2}$), 724.0 ($\text{Fe}^{2+} 2p_{1/2}$) and 726.3 eV ($\text{Fe}^{3+} 2p_{1/2}$)^[39]. By estimating the area ratio (S) of the characteristic peaks of Fe^{3+} , $S(\text{Fe}^{3+})/S(\text{Fe}^{2+} + \text{Fe}^{3+})$, we calculated the relative contents of Fe for both samples [Supplementary Table 2]. Deconvolution of the Fe 2p XPS of $\gamma\text{-Fe}_2\text{O}_3$ and 27% Mo- Fe_2O_3 [Figure 3A and Supplementary Table 2] demonstrates that the molar ratio of Fe^{3+} increases obviously after Mo doping, which is beneficial for improving the structural stability of $\gamma\text{-Fe}_2\text{O}_3$ ^[40]. Figure 3B shows the O 1s spectra of $\gamma\text{-Fe}_2\text{O}_3$ and 27% Mo- Fe_2O_3 , which are fitted into three characteristic peaks at 532.5, 530.9 and 529.4 eV, corresponding to adsorbed oxygen species (O_γ), oxygen vacancies (O_β), and lattice oxygen (O_α), respectively^[41]. According to the area ratio of the characteristic peaks provided in Supplementary Table 2, the increase of O_α concentration proves that Mo atoms have successfully occupied the Fe sites in the $\gamma\text{-Fe}_2\text{O}_3$ lattice^[42]. The decrease of O_β concentration is conducive to capturing photogenerated electrons and inhibiting the recombination of photogenerated carriers^[43]. The concentration of O_γ , increasing from 14.62% to 16.62% after Mo doping, is beneficial for the generation of superoxide anion radicals ($\cdot\text{O}_2^-$) at the photoelectrode and promoting the PEC degradation of TC^[44]. Furthermore, the electronic states of the Mo species of MoO_3 and 27% Mo- Fe_2O_3 were also determined by Mo 3d XPS [Supplementary Figure 3]. Obviously, the Mo species of 27% Mo- Fe_2O_3 are dominantly Mo^{5+} , as judged by the binding energies of the Mo 3d peaks of MoO_3 and 27% Mo- Fe_2O_3 , due to the same ionic radius (in Supplementary Table 3) of Mo^{5+} and Fe^{2+} . By combining the above XRD and HAADF-STEM results, it is convincing that the Mo species are incorporated into the lattice of $\gamma\text{-Fe}_2\text{O}_3$, leading to the strong electron interaction between Fe and Mo.

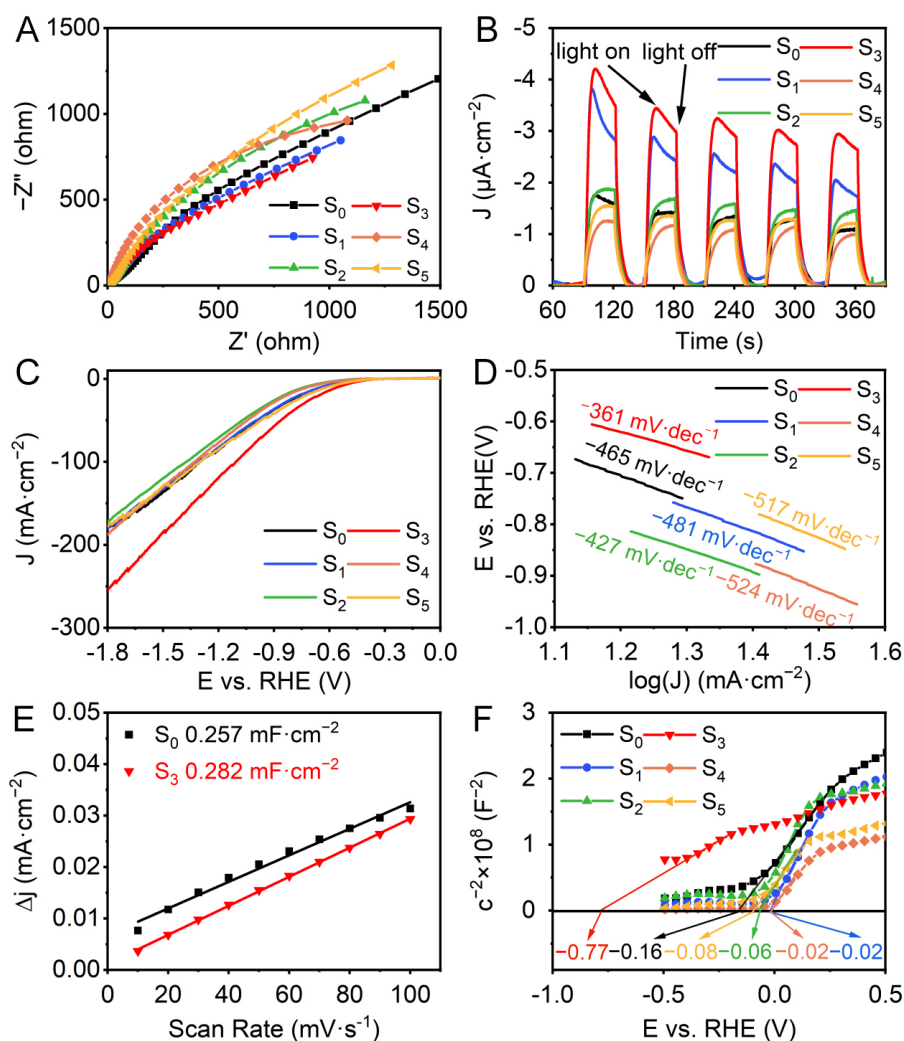


Figure 4. (A) Nyquist plots under AM 1.5 G illumination, (B) photocurrent responses, (C) LSV curves under AM 1.5 G illumination, (D) Tafel plots, (E) C_{dl} , (F) Mott-Schottky plots of S_0 , S_{17} , S_{27} , S_{37} , S_{45} and S_{55} . LSV: Linear sweep voltammogram; AM 1.5 G: air mass 1.5 global solar spectrum; RHE: reversible hydrogen electrode.

Figure 4 displays the Nyquist plots of photocathodes, which further reveal the influence of the doping amount of Mo on the charge transfer process. The smaller diameter of capacitive loop in the Nyquist plot means the lower charge transfer resistance (R_{ct}) and the higher separation efficiency of photogenerated charges^[45]. As shown in Figure 4A, 27% Mo-Fe₂O₃ shows the smallest arc radius, meaning it has the smallest resistance at the electrolyte interface and the best photoelectric properties, owing to the interaction between Mo and Fe, which promotes the charge transfer at the electrolyte interface. Transient photocurrent testing was employed to further evaluate the superiority of charge transfer on the Mo-Fe₂O₃ electrode. In Figure 4B, the photocurrent density of 27% Mo-Fe₂O₃ is $-3.45 \mu\text{A}\cdot\text{cm}^{-2}$, 2.35 times higher than that of $\gamma\text{-Fe}_2\text{O}_3$ ($-1.47 \mu\text{A}\cdot\text{cm}^{-2}$), verifying the introduction of Mo doping effectively facilitates the separation of photogenerated charges in $\gamma\text{-Fe}_2\text{O}_3$. Figure 4C presents the excellent photocurrent density of 27% Mo-Fe₂O₃ photocathode, $-184 \text{ mA}\cdot\text{cm}^{-2}$ at -1.5 V (vs. RHE), reaching 39.4% enhancement compared to $\gamma\text{-Fe}_2\text{O}_3$. As shown in Figure 4D, the Tafel slopes of $\gamma\text{-Fe}_2\text{O}_3$, 9% Mo-Fe₂O₃, 18% Mo-Fe₂O₃, 27% Mo-Fe₂O₃, 36% Mo-Fe₂O₃, and 45% Mo-Fe₂O₃ are -465 , -481 , -427 , -361 , -524 , and $-517 \text{ mV}\cdot\text{dec}^{-1}$, respectively, in which 27% Mo-Fe₂O₃ displays the smallest Tafel slope, indicating it possesses the fastest reaction kinetics. This is because an optimal electronic interactions between Mo and Fe in 27% Mo-Fe₂O₃, which optimizes the electronic conductivity of the material and significantly reduces the reaction energy barrier. To characterize the active

sites of the catalysts, the electrochemical active surface areas of $\gamma\text{-Fe}_2\text{O}_3$ and 27% Mo- Fe_2O_3 were measured by the C_{dl} . The current density difference (Δj) at 0.715 V (*vs.* RHE) is plotted against different scan rates ranging from 10 $\text{mV}\cdot\text{s}^{-1}$ to 100 $\text{mV}\cdot\text{s}^{-1}$ to obtain C_{dl} [Figure 4E and Supplementary Figure 4]. The C_{dl} values of $\gamma\text{-Fe}_2\text{O}_3$ and 27% Mo- Fe_2O_3 were 0.257 and 0.282 $\text{mF}\cdot\text{cm}^{-2}$, respectively, indicating that 27% Mo- Fe_2O_3 can provide more active sites during PEC reactions. The Mott-Schottky test is conducted to determine the semiconductor type, the carrier concentration, and the flat band potential. Therefore, we measured the Mott-Schottky curves at a frequency of 1,000 Hz for $\gamma\text{-Fe}_2\text{O}_3$ and $x\%$ Mo- Fe_2O_3 samples under dark conditions to obtain the conductor types and further explore the charge separation process on the electronic properties. As shown in Figure 4F, all the samples exhibit positive slopes, indicating they are all typical n-type semiconductors^[46]. By extending the straight line to the x -axis, the intercept gives the value of the flat band potential which is approximately equal to the conduction band (CB) position. The CB positions of $\gamma\text{-Fe}_2\text{O}_3$, 9% Mo- Fe_2O_3 , 18% Mo- Fe_2O_3 , 27% Mo- Fe_2O_3 , 36% Mo- Fe_2O_3 and 45% Mo- Fe_2O_3 are -0.16, -0.02, -0.06, -0.77, -0.02, and -0.06 V (*vs.* RHE), respectively, in which 27% Mo- Fe_2O_3 has the most negative CB potential and thus presents the strongest reduction ability.

As shown in Supplementary Figure 5, UV-vis diffuse reflectance spectroscopy reveals that the optical band gaps of $\gamma\text{-Fe}_2\text{O}_3$ and the Mo- Fe_2O_3 samples with different Mo doping amounts are 1.98, 1.94, 1.95, 1.98, 2.01, and 2.02 eV, respectively, indicating that the introduction of Mo atoms does not significantly alter the intrinsic light absorption edge of $\gamma\text{-Fe}_2\text{O}_3$. Combined with the results of EIS and photocurrent density, the 27% Mo- Fe_2O_3 exhibits optimized surface photoelectrochemical properties after Mo doping, which is beneficial for promoting the PEC process.

The valence band edges of $\gamma\text{-Fe}_2\text{O}_3$ and 27% Mo- Fe_2O_3 were measured by valence-band XPS [Supplementary Figure 6A]. The VBM was determined by linear extrapolation of the leading edge of the spectra. The VBM values are 0.70 and 0.60 eV for $\gamma\text{-Fe}_2\text{O}_3$ and 27% Mo- Fe_2O_3 , respectively. The work functions of the two samples were further characterized by UPS, as shown in Supplementary Figure 6B and C. The work function decreases from 3.56 eV for $\gamma\text{-Fe}_2\text{O}_3$ to 3.45 eV upon Mo doping. The concurrent decrease in both VBM and work function indicates that the incorporation of Mo elevates the surface Fermi level of $\gamma\text{-Fe}_2\text{O}_3$, inducing a downward band bending of approximately 0.1 eV and forming an electron-accumulation layer at the surface. This electronic modification lowers the thermodynamic barrier for photoexcited electrons to migrate from the bulk to the surface and further into vacuum^[33], thereby facilitating charge transfer to the surface. In combination with the LSV results, the observed band structure engineering well explains why 27% Mo- Fe_2O_3 exhibits a significantly higher photocurrent density than $\gamma\text{-Fe}_2\text{O}_3$.

Finally, the PEC degradation of TC using the as-prepared photocathodes were evaluated. As shown in Figure 5A, 27% Mo- Fe_2O_3 reaches the removal efficiency of 100% in 25 min, while other catalysts achieve the removal efficiency of 100% in 30 min. The first-order rate constant (k) for the reaction was determined using the equation $\ln(C_0/C_t) = kt$, where C_0 is the initial TC concentration and C_t is the concentration at time t ^[47]. All degradation experiments were performed three times, and the reported k values are the averages of three independent measurements. The k values of $\gamma\text{-Fe}_2\text{O}_3$, 9% Mo- Fe_2O_3 , 18% Mo- Fe_2O_3 , 27% Mo- Fe_2O_3 , 36% Mo- Fe_2O_3 , 45% Mo- Fe_2O_3 are 0.245, 0.214, 0.174, 0.294, 0.199 and 0.172 min^{-1} , respectively [Figure 5B]. The recycling PEC degradation experiments of TC by 27% Mo- Fe_2O_3 are shown in Figure 5C, quite important for the catalysts. The 27% Mo- Fe_2O_3 still achieved the removal efficiency of 100% in 30 min after 5 consecutive cycles. In addition, the PEC degradation of TC with high initial concentration by 27% Mo- Fe_2O_3 were also investigated [Supplementary Figure 7]. When TC initial concentration increased to 50 and 100 $\text{mg}\cdot\text{L}^{-1}$, the removal efficiency of TC after 30 min decreased to 86.32% and 67.76%, respectively, which may be attributed to competitive adsorption and accumulation of intermediate products occupying the active sites. The superior PEC property of 27% Mo- Fe_2O_3 could be attributed to the strong interaction between Mo and Fe,

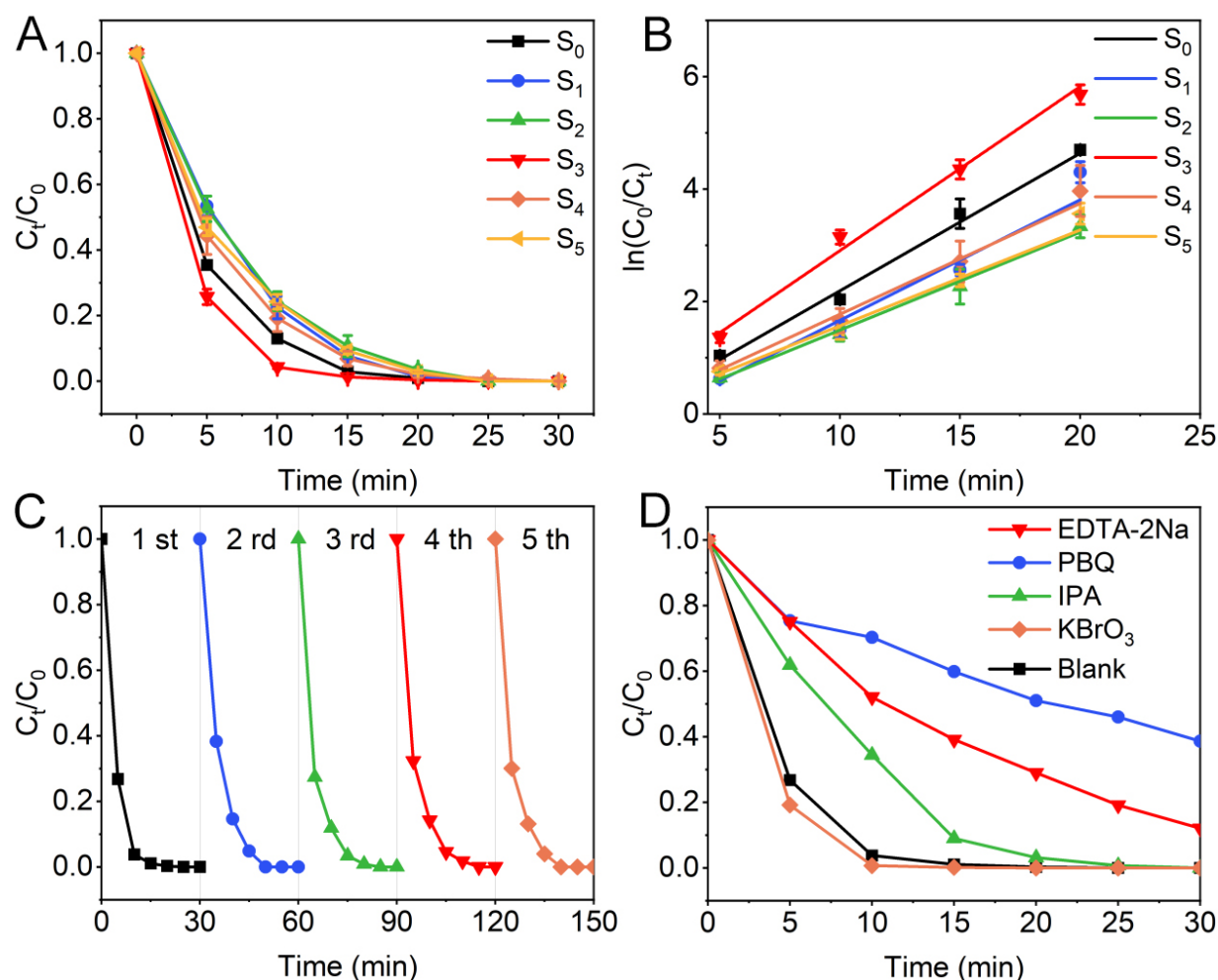


Figure 5. (A) PEC degradation of TC under simulated sunlight by catalysts and (B) the corresponding kinetic linear simulation curves; (C) Recycling PEC degradation of TC by 27% Mo-Fe₂O₃; (D) The influence of different quenchers on the PEC degradation of TC by 27% Mo-Fe₂O₃. Error bars in the corresponding figures represent the SD of three independent measurements. TC: Tetracycline; PEC: photoelectrocatalytic; SD: standard deviation; PBQ: p-benzoquinone; IPA: isopropanol; EDTA-2Na: ethylenediaminetetraacetic acid disodium salt dihydrate.

which can promote the separation and migration of photogenerated carriers, and then react with the adsorbed reactants effectively. To elucidate the reaction mechanism, the main active groups in the photocatalytic degradation of TC using 27% Mo-Fe₂O₃ were conducted by radical capture experiment [Figure 5D]. Four different quenchers (5 mmol·L⁻¹ each) were used to target specific active species: PBQ can capture superoxide anion ($\cdot\text{O}_2^-$), IPA can capture hydroxyl radical ($\cdot\text{OH}$), EDTA-2Na can capture holes (h^+), and KBrO₃ can capture electron (e^-). The removal rate of TC decreases significantly in the presence of PBQ, suggesting that $\cdot\text{O}_2^-$ is the primary active species. Secondly, the removal rate of TC decreases moderately in the presence of EDTA-2Na and IPA, implying that h^+ and $\cdot\text{OH}$ are the secondary active species. In contrast, KBrO₃ has little impact on the removal rate, indicating that e^- is not the main active species.

To shed light on the possible degradation pathways of TC by 27% Mo-Fe₂O₃, we conducted a test on the reaction intermediates employing LC-MS analysis [Supplementary Figure 8] and proposed two possible degradation pathways mainly driven by the synergistic action of $\cdot\text{O}_2^-$ and h^+ according to Figure 6. The TC

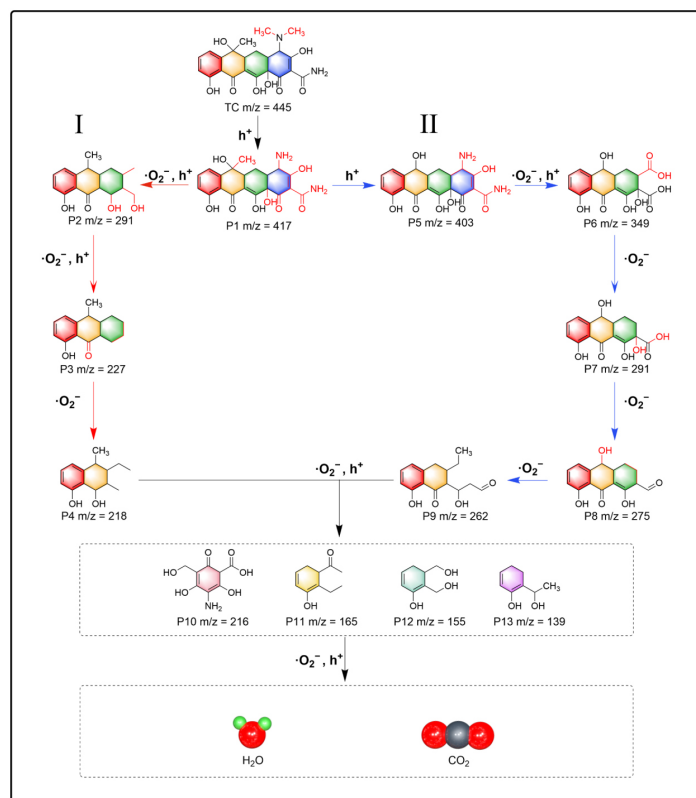


Figure 6. Possible degradation pathways of TC by 27% Mo-Fe₂O₃. TC: Tetracycline.

molecule ($m/z = 445$) initially is attacked by h^+ , yielding demethylation intermediate P1 ($m/z = 417$)^[20]. Subsequently, intermediate P1 undergoes a ring-opening reaction to generate intermediate P2 ($m/z = 291$) and at the same time undergoes demethylation to form intermediate P5 ($m/z = 403$), respectively, which correspond respectively to reaction pathways I and II. In pathway I, intermediate P2 transforms into P3 ($m/z = 227$) after undergoing simultaneous elimination of $-CH_3$, $-OH$ and $-CH_2OH$ groups, then P3 undergoes a ring-opening reaction to generate P4 ($m/z = 218$). While in pathway II, intermediate P5 ($m/z = 403$) loses $-OH$ and $-NH_2$ under the concerted action of $\cdot O_2^-$ and h^+ to yield P6 ($m/z = 349$). P6 undergoes elimination of a $-COOH$ mediated by $\cdot O_2^-$ to form P7 ($m/z = 291$). Subsequently, P7 loses $-OH$ to form P8 ($m/z = 275$). Thereafter, P8 undergoes ring-opening with $\cdot O_2^-$ to yield P9 ($m/z = 262$). The intermediates (P4 and P9) progressively convert into smaller molecular intermediates (P10, P11, P12, P13) under the continuous action of $\cdot O_2^-$ and h^+ , and finally generate harmless substances CO₂ and H₂O.

Based on the above results, we propose the possible PEC mechanism of 27% Mo-Fe₂O₃ [Figure 7], including the oxidation reaction at the anode and the reduction reaction at the cathode. When the photocathode absorbs solar energy, photogenerated electrons (e^-) transition to the CB, leaving holes (h^+) in the valence band (VB) at the same time. Under an applied external bias potential, e^- flow to the cathode through the external circuit, while h^+ migrate to the surface of the photocathode^[48]. A portion of the h^+ recombine with electrons, while the remaining h^+ participate in reactions. On the one hand, h^+ can directly undergo oxidation reactions with the TC molecules adsorbed on the surface of the photocathode, thereby decomposing TC. On the other hand, h^+ can also react with the electrolytes in the solution, generating corresponding active free radicals (such as $\cdot OH$) and participating in the oxidation of TC indirectly^[49]. The dissolved O₂ in the solution can also capture e^- to generate active species such as $\cdot O_2^-$, thereby participating in the degradation process of TC. This path effectively separates the photogenerated electrons and holes and meanwhile inhibits their recombination, resulting in excellent PEC activity.

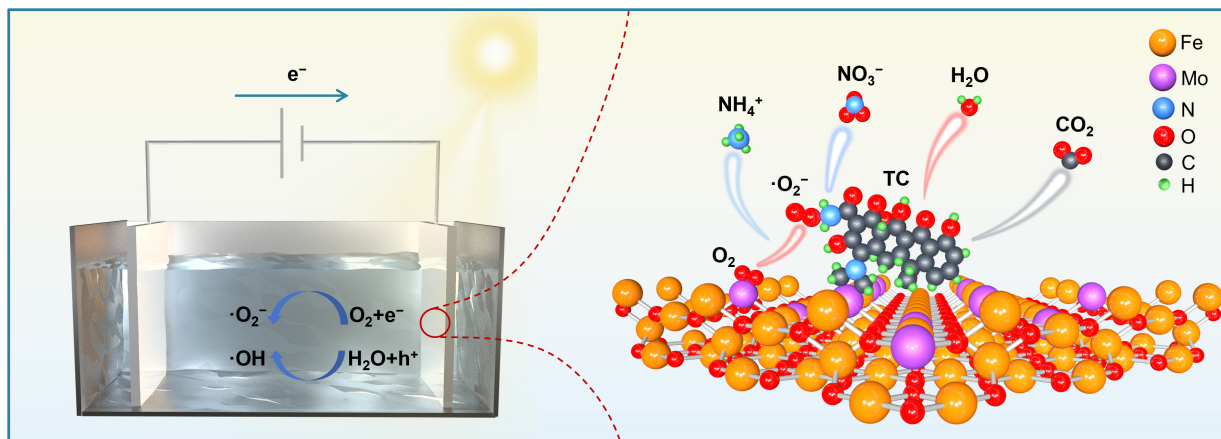


Figure 7. Schematic description of the PEC mechanism of 27% Mo- Fe_2O_3 . PEC: Photoelectrocatalytic.

CONCLUSIONS

In summary, Mo-doped γ - Fe_2O_3 was successfully synthesized via a facile co-precipitation combined with impregnation method. Combined with the analysis of XRD, XPS, TEM-EDS mapping and HAADF-STEM, Mo atoms are doped into the lattice of γ - Fe_2O_3 . And the modification of Mo doping has an impact on the electronic structure of γ - Fe_2O_3 , facilitating the separation and migration of photogenerated carriers, and resulting in superior PEC activity. Herein, we provide a feasible strategy for developing doped catalysts with superior PEC performance by enhancing the electronic interactions.

DECLARATIONS

Authors' contributions

Chemical syntheses and characterizations: Xia, X.; Zhang, Z.; Jia, P.

Data analysis and interpretation: Xia, X.; Liu, X.

Topic selection, manuscript review: Liu, X.; Liu, Z.

Editing and supervision: Wang, H.; Liu, W.

All authors contributed to the discussion of results and the manuscript writing.

Availability of data and materials

Some results of supporting the study are presented in the [Supplementary Materials](#). Other raw data that support the findings of this study are available from the corresponding author upon reasonable request.

AI and AI-assisted technologies statement

Not applicable.

Financial support and sponsorship

This research was funded by the National Natural Science Foundation of China (No. 22006082 and 52172147), Major scientific research special projects for the construction of national key laboratories (No. 2025ZDGZ02), the Natural Science Foundation of Shandong Province (No. ZR2022MB095 and ZR2021MB035), and Development Project of Youth Innovation Teams in Colleges and Universities of Shandong Province (Grant No. 2022KJ293).

Conflict of interest

Liu, Z. is affiliated with Shandong Environmental Protection Development Group Co., Ltd., Jinan 250101, China, but this affiliation did not influence the research or its outcomes. The other authors declared that there are no conflicts of interest.

Ethical approval and consent to participate

Not applicable.

Consent for publication

Not applicable.

Copyright

© The Author(s) 2026.

Supplementary Materials

[Supplementary Materials](#)

REFERENCES

1. Xu, M.; Wang, Q.; Maqbool, T.; Guo, B.; Lu, H.; Jiang, D. Contrasting responses of antibiotic resistance genes (ARGs) to biocathodic and bioanodic treatment of broad-spectrum tetracycline and narrow-spectrum fidaxomicin. *Chem. Eng. J.* **2025**, *515*, 163878. DOI
2. Li, Q.; Zheng, Y.; Guo, L.; et al. Microbial degradation of tetracycline antibiotics: mechanisms and environmental implications. *J. Agric. Food. Chem.* **2024**, *72*, 13523-36. DOI
3. Zong, Z.; Huang, Y.; Kwan, J.; Hankins, N. P. Standardized benchmarking of advanced oxidation processes for tetracycline degradation with life cycle assessment and economic evaluation. *Chem. Eng. J.* **2025**, *525*, 170664. DOI
4. Zeng, S.; Chen, Y.; Zhang, N.; et al. Tetracycline effects on arsenate reduction in agricultural soils under different soil water contents. *Environ. Pollut.* **2026**, *389*, 127398. DOI
5. Daghrir, R.; Drogui, P. Tetracycline antibiotics in the environment: a review. *Environ. Chem. Lett.* **2013**, *11*, 209-27. DOI
6. Fan, Y.; Liu, D.; Wan, H.; Liu, X.; Wang, J.; Xiong, K. Enhanced double-exchange interactions enable the Co and Mn co-doped zinc ferrite rapid and efficient removal of tetracycline. *J. Environ. Chem. Eng.* **2025**, *13*, 117070. DOI
7. Liang, S.; Zhang, H.; Dai, H.; et al. Efficient, rapid and simple adsorption method by polydopamine polystyrene nanofibers mat for removal of multi-class antibiotic residues in environmental water. *Chemosphere* **2022**, *288*, 132616. DOI
8. Scaria, J.; Anupama, K.; Nidheesh, P. Tetracyclines in the environment: an overview on the occurrence, fate, toxicity, detection, removal methods, and sludge management. *Sci. Total. Environ.* **2021**, *771*, 145291. DOI
9. Song, C.; Sun, X.; Xia, P.; Wang, Y.; Wang, S. Investigation of fate and behavior of tetracycline in nitrifying sludge system. *RSC. Adv.* **2015**, *5*, 87333-40. DOI
10. Zhang, Y.; Huang, X.; Zheng, Q.; Yang, J.; Zhai, L.; Song, Y. Spherical Bi₄O₅I₂/MoS₂ QDs nanocomposites activate persulfate to degrade tetracycline under visible light. *Adv. Sustain. Syst.* **2023**, *8*, 2300439. DOI
11. Kumar, A.; Choudhary, P.; Kumar, A.; Camargo, P. H. C.; Krishnan, V. Recent advances in plasmonic photocatalysis based on TiO₂ and noble metal nanoparticles for energy conversion, environmental remediation, and organic synthesis. *Small* **2021**, *18*, 2101638. DOI
12. Wang, Z.; Meng, S.; Li, J.; et al. Oxygen Vacancy engineering and constructing built-in electric field in Fe-g-C₃N₄/Bi₂MoO₆ Z-scheme heterojunction for boosting photo-fenton catalytic degradation performance of tetracycline. *Small* **2024**, *20*, 2406125. DOI
13. Li, J.; Cai, L.; Shang, J.; Yu, Y.; Zhang, L. Giant Enhancement of internal electric field boosting bulk charge separation for photocatalysis. *Adv. Mater.* **2016**, *28*, 4059-64. DOI
14. Li, J.; Zhang, X.; Xiong, X.; Wu, C.; Jin, Y.; Lv, K. Breaking Type-I heterojunction limitations: harnessing an ohmic-like/S-scheme cascade charge transfer mechanism for enhanced photocatalytic H₂ evolution. *Sep. Purif. Technol.* **2025**, *354*, 129444. DOI
15. Yu, H.; Xu, J.; Liu, H.; et al. Defect synergy enabled by spin-polarization-tunable engineering for enhanced photocatalysis: carrier migration mechanisms. *Chem. Eng. J.* **2025**, *523*, 168394. DOI
16. Li, C.; Wu, M.; Lei, J.; et al. Work-function-driven built-in electric field in flame-synthesized BiVO₄ QDs/TiO₂ composites: a high-efficiency photoelectrocatalytic platform for continuous flow degradation of tetracycline in wastewater. *J. Environ. Chem. Eng.* **2025**, *13*, 118655. DOI
17. Adak, D.; Chakrabarty, P.; Majumdar, P.; et al. Pd nanoparticle-decorated hydrogen plasma-treated TiO₂ for photoelectrocatalysis-based solar energy devices. *ACS. Appl. Electron. Mater.* **2020**, *2*, 3936-45. DOI
18. Wu, H.; Liu, Q.; Zhang, L.; Tang, Y.; Wang, G.; Mao, G. Novel nanostructured WO₃@prussian blue heterojunction photoanodes for efficient photoelectrochemical water splitting. *ACS. Appl. Energy. Mater.* **2021**, *4*, 12508-14. DOI
19. Wang, R.; Chen, S.; Ng, Y. H.; et al. ZnO/CdS/PbS nanotube arrays with multi-heterojunctions for efficient visible-light-driven photoelectrochemical hydrogen evolution. *Chem. Eng. J.* **2019**, *362*, 658-66. DOI
20. He, S.; Yan, C.; Chen, X.; et al. Construction of core-shell heterojunction regulating α -Fe₂O₃ layer on CeO₂ nanotube arrays enables highly efficient Z-scheme photoelectrocatalysis. *Appl. Catal. B. Environ.* **2020**, *276*, 119138. DOI
21. Chen, Y.; Lin, M.; Peng, Z.; et al. Fabrication of piezotronic ZnO p-n homojunction via metal/oxygen defects modulation for efficient photoelectrocatalysis. *Chem. Eng. Sci.* **2024**, *295*, 120174. DOI

-
22. Li, Y.; Yu, L.; Xie, J.; et al. Efficient photoelectrocatalytic degradation of tetracycline coupled with hydrogen production by N-doped carbon layer-wrapped TiO₂ nanorods. *J. Environ. Chem. Eng.* **2025**, *13*, 115153. DOI
 23. Yu, J.; Su, Q.; Huang, J.; Teng, W.; Song, Y.; Zhang, H. Synergistic interfacial engineering of S-scheme 2H-MoSe₂/NiFe-LDH architecture for dual functional photoelectrocatalysis: multi-pollutant mineralization and visible light driven hydrogen evolution. *Chem. Eng. J.* **2025**, *519*, 164914. DOI
 24. Liu, J.; Liang, R.; Hu, Z.; Zhang, X.; Zhou, M. Photoelectrocatalysis/photoelectro-fenton system based on cone-like TiO₂/nickel foam photoanode for efficient degradation of carbamazepine: comparison with DSA. *Chem. Eng. J.* **2024**, *491*, 152088. DOI
 25. Li, B.; Lv, M.; Zhang, Y.; et al. Single-particle imaging photoinduced charge transfer of ferroelectric polarized heterostructures for photocatalysis. *ACS. Nano.* **2024**, *18*, 25522-34. DOI
 26. Vaghasiya, J. V.; Mayorga-martinez, C. C.; Zelenka, J.; Sharma, S.; Ruml, T.; Pumera, M. Magnetic soft centirobot to mitigate biological threats. *SmartMat* **2024**, *5*, e1289. DOI
 27. Hu, H.; Zhang, C.; Qi, H.; et al. Seawater electrosynthesis of hydrogen peroxide at industrial-level current densities enabled by pentagonal defect-rich nanocarbon with chlorine doping. *Angew. Chem. Int. Ed.* **2025**, *65*, e12138. DOI
 28. Wong, K. J.; Foo, J. J.; Siang, T. J.; Ong, W. J. Transition metal carbide-based photocatalysts for artificial photosynthesis. *SmartMat* **2023**, *5*, e1238. DOI
 29. Kahng, S.; Kim, J. H. Heterojunction photoanode of SnO₂ and Mo-doped BiVO₄ for boosting photoelectrochemical performance and tetracycline hydrochloride degradation. *Chemosphere* **2022**, *291*, 132800. DOI
 30. Zhang, X.; Xu, C.; Yu, C.; et al. Oxygen vacancy defect engineering in MoO₂/Mo-doped BiOCl ohmic junctions for enhanced photocatalytic antibiotic elimination. *J. Alloys. Compd.* **2024**, *1005*, 176220. DOI
 31. Qu, W.; Chen, Y.; Huang, Z.; et al. Active tetrahedral iron sites of γ -Fe₂O₃ catalyzing NO reduction by NH₃. *Environ. Sci. Technol. Lett.* **2017**, *4*, 246-50. DOI
 32. Zheng, J.; Xu, S.; Sun, J.; et al. Boosting efficient C-N bonding toward photoelectrocatalytic urea synthesis from CO₂ and nitrate via close Cu/Ti bimetallic sites. *Appl. Catal. B. Environ.* **2023**, *338*, 123056. DOI
 33. De La Fuente, B.; Bomnater, J.; Del Moro, M.; et al. On the combination of ultraviolet photoelectron spectroscopy with optical absorption studies to investigate Cu₂O||TiO₂ direct Z-scheme junctions with different Cu₂O loading. *Appl. Surf. Sci.* **2024**, *657*, 159796. DOI
 34. Han, S.; Hu, X.; Wang, J.; Fang, X.; Zhu, Y. Novel route to Fe-based cathode as an efficient bifunctional catalysts for rechargeable Zn-air battery. *Adv. Energy. Mater.* **2018**, *8*, 1800955. DOI
 35. Cheng, L.; Jiang, T.; Yan, K.; Gong, J.; Zhang, J. A dual-cathode photoelectrocatalysis-electroenzymatic catalysis system by coupling BiVO₄ photoanode with hemin/Cu and carbon cloth cathodes for degradation of tetracycline. *Electrochim. Acta.* **2019**, *298*, 561-9. DOI
 36. Al Huwayz, M.; Tahir, A.; Alomairy, S.; et al. RETRACTED: Harnessing the interfacial charge transfer in Mn-doped γ -Fe₂O₃@ZnO heterojunction for broad spectrum photocatalytic degradation of organic dyes. *Opt. Mater.* **2024**, *157*, 116348. DOI
 37. Shannon, R. D. Revised effective ionic radii and systematic studies of interatomic distances in halides and chalcogenides. *Acta. Cryst. A.* **1976**, *32*, 751-67. DOI
 38. Liu, J.; Hu, J.; Han, X.; et al. Simple synthesis of low-load γ -Fe₂O₃/C/CNT for efficient building absorber. *Mater. Today. Commun.* **2025**, *46*, 112529. DOI
 39. Chen, Y.; Liu, L.; Zhang, L.; et al. Construction of Z-type heterojunction BiVO₄/Sm/ α -Fe₂O₃ photoanode for selective degradation: efficient removal of bisphenol A based on multifunctional Sm-doped modification. *Appl. Catal. B. Environ. Energy.* **2023**, *333*, 122775. DOI
 40. Hsu, J. H.; Kuo, P. C.; Hsu, C. W. Improved thermal stability of Mo-modified γ -Fe₂O₃ particles. *J. Appl. Phys.* **1990**, *67*, 5152-4. DOI
 41. Lu, L.; Xin, Z.; Wang, X.; et al. KOH-modified Ni/LaTiO₂N Schottky junction efficiently reducing CO₂ to CH₄ under visible light irradiation. *Appl. Catal. B. Environ.* **2019**, *244*, 786-94. DOI
 42. Zheng, Y.; Hussain, G.; Zheng, C.; et al. Impact of the rhenium substitution on the oxygen evolution reaction of spinel CoFe₂O₄. *J. Mater. Chem. A.* **2024**, *12*, 19521-31. DOI
 43. Wei, X.; Yang, Y.; Li, S.; Meng, Y.; Yuan, W.; Ni, H. Dual role of oxygen vacancies in TiO₂/Bi₂O₃ for enhanced carrier separation and PDS activation: a combined experimental and DFT study. *Environ. Res.* **2025**, *282*, 122042. DOI
 44. Li, J.; Tang, H.; Liu, C.; et al. Selective generation of superoxide radical for de-NO_x via fly ash/H₂O₂ slurry: unveiling the role of surface hydroxyls for H₂O₂ activation. *Sep. Purif. Technol.* **2025**, *379*, 135081. DOI
 45. Guardiano, M. G.; Gonzaga, I. M. D.; Ribeiro, L. K.; Almeida, C. V. D. S.; Mascaro, L. H. Gd-BiVO₄: an efficient photoanode for pharmaceuticals degradation in contaminated waters via solar photoelectrocatalysis. *Chem. Eng. J.* **2025**, *503*, 158463. DOI

-
46. Ma, L.; Lu, M.; Li, K.; et al. Photocatalytic degradation of octadecylamine and 4-dodecylmorpholine over titanium based photocatalyst: activity and mechanism insights. *Chem. Eng. J.* **2023**, *472*, 144782. DOI
 47. Zhong, X.; Li, L.; Xiang, W.; et al. Stable and rapid degradation of tetracycline using a photoelectrochemical system comprising a Ag/N-TiO₂ photoanode and P-Pd cathode. *J. Environ. Chem. Eng.* **2023**, *11*, 109875. DOI
 48. Ren, M.; Lu, H.; Liu, Z.; et al. Synergistic antibiotic degradation by polydopamine/BiOBr-modified photocathode in self-powered photo-bio-electrochemical system. *Bioresour. Technol.* **2026**, *442*, 133669. DOI
 49. Zhang, X.; Yu, W.; Guo, Y.; et al. Recent advances in photoelectrocatalytic advanced oxidation processes: From mechanism understanding to catalyst design and actual applications. *Chem. Eng. J.* **2023**, *455*, 140801. DOI

Disclaimer/Publisher's Note: All statements, opinions, and data contained in this publication are solely those of the individual author(s) and contributor(s) and do not necessarily reflect those of OAE and/or the editor(s). OAE and/or the editor(s) disclaim any responsibility for harm to persons or property resulting from the use of any ideas, methods, instructions, or products mentioned in the content.



© The Author(s) 2026. Open Access This article is licensed under a Creative Commons Attribution 4.0 International License (<https://creativecommons.org/licenses/by/4.0/>), which permits unrestricted use, sharing, adaptation, distribution and reproduction in any medium or format, for any purpose, even commercially, as long as you give appropriate credit to the original author(s) and the source, provide a link to the Creative Commons license, and indicate if changes were made.